npj | natural hazards

Article

https://doi.org/10.1038/s44304-026-00186-8

Climate extremes and urbanization drive flood tipping points at the city–river interface

Dingyu Xuan[1,2] ✉, M. Ani Hsieh[3,4], Leandro S. Pongeluppe[5], Mackenzie M. Weaver[1], Michael E. Mann[1], Douglas J. Jerolmack[1,4] & Hugo N. Ulloa[1] ✉

Hurricane Ida struck the U.S. East Coast in August 2021, driving the Schuylkill River in Philadelphia to a record discharge nearly 100 times its average flow. Ida exposes the growing challenge of predicting urban flooding arising from coupled rainfall–runoff and river–tide–landscape interactions that coarse models cannot resolve. Here, we address this gap with a street-resolving flood model that integrates LiDAR-derived terrain, bathymetric surveys, and land-use-based surface friction across Philadelphia's watershed to reproduce Ida's flood. We show that soil saturation, impervious surfaces, and fragmented infrastructure amplify pluvial flooding, increasing exposure in both low- and high-income communities. Scenario simulations reveal a flood tipping point: for river return periods exceeding 100 years, the inundated area grows logarithmically, with an additional 2–7% increase in flooding when peak discharge coincides with high tide and up to ~15% under projected sea-level rise by 2100. As extreme rainfall intensifies and return periods shorten, this tipping point will be crossed more often, demanding integrated forecasting and adaptive planning in vulnerable, low-lying, rapidly urbanizing regions.

Hurricane Ida made landfall in Louisiana as a Category 4 hurricane on August 29, 2021, producing strong winds, storm surges, and intense rainfall that devastated the Gulf Coast[1]. As it moved inland (SI Fig. S1), the storm's remnants and seven tornadoes that struck Philadelphia between September 1–2 triggered unprecedented discharge and a 1-in-100-year flood along the Schuylkill River, causing widespread damage[2] (SI Table S2). Extreme hydrometeorological events (EHMEs) like Ida already cause average global losses of $136.7 billion annually (2003–2022)[3], surging to over $320 billion in 2024 alone[4]. Rain-driven floods are projected to intensify as climate extremes intensify and urbanization expands, thereby constraining rivers and altering floodplain dynamics[5,6]. In tidally influenced rivers, sea-level rise (SLR) and stronger tropical cyclones further amplify flood severity and human vulnerability[7,8]. Currently, 13.3% of the U.S. population—over 40 million people—is exposed to a 1-in-100-year flood[9], yet future flood risks in urban and coastal corridors remain poorly quantified[10,11], relying on coarse models that obscure critical compound drivers and limit effective mitigation in densely populated metropolitan regions[12]. Philadelphia exemplifies this challenge: as the second-most populous city on the U.S. East Coast (1.5M), bounded by the Delaware River to the east and bisected by the Lower Schuylkill River (Fig. 1a–c).

The Schuylkill River rushes through bedrock rapids as it enters Philadelphia, transitioning from the Piedmont to the Coastal Plain, where urban development is concentrated[13]. Historically, the Schuylkill served as both a sewer and a navigable waterway during the 19th century, supporting Philadelphia's rapid industrial and population growth from around 41,000 residents in 1800 to nearly 1.3 million by 1900[13]. By the 20th century, flood-control measures—channelization and levee construction—were introduced to reduce mounting flood risks[14], such as the Fairmount Dam. These interventions enabled dense riverside development but also severed the river's connection to its natural floodplain, diminishing its ability to absorb and regulate extreme events. Meanwhile, average annual discharge of the river (25–160 m^3/s) has increased since 1931 with a modest yet statistically significant rising trend (0.3 $m^3/s/a$) (SI Fig. S2a), typically peaking in spring but now showing more frequent and extreme autumn peaks from hurricane intensification under climate change[15,16] (SI Fig. S2b). Current infrastructure struggles with intensifying EHMEs, as demonstrated by Hurricane Ida. A broader knowledge gap persists in understanding how urban rivers, particularly those tidally influenced, respond to compounding stressors such as EHMEs and SLR. This challenge extends far beyond Philadelphia, affecting cities worldwide where fluvial–tidal interactions remain poorly understood

[1]Department of Earth and Environmental Science, University of Pennsylvania, Philadelphia, PA, USA. [2]Department of Civil and Environmental Engineering, Imperial College London, London, UK. [3]General Robotics, Automation, Sensing, and Perception (GRASP) Lab, University of Pennsylvania, Philadelphia, PA, USA. [4]Department of Mechanical Engineering and Applied Mechanics, University of Pennsylvania, Philadelphia, PA, USA. [5]The Wharton School, University of Pennsylvania, Philadelphia, PA, USA. ✉e-mail: dingyu.xuan24@imperial.ac.uk; ulloa@sas.upenn.edu

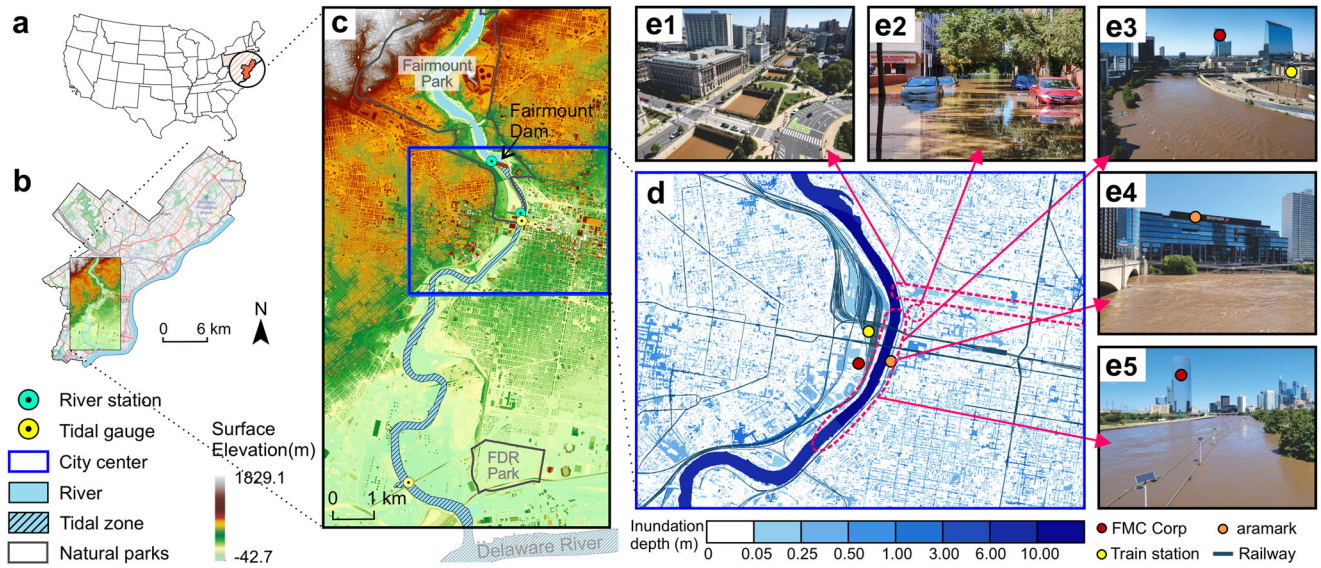

Fig. 1 | Map of research area and flood inundation of the Center City validated by drone images. **a** The location of Philadelphia in the US. **b** Research area in Philadelphia overlaid with Open Street Map. **c** Surface elevation of the study area. **d** Flood inundation map based on the Digital Surface Model (DSM) with railway lines overlaid. **e** Drone images with identifiable landmarks were collected from social media, illustrating the actual inundated areas: **e1** Vine Street Expressway; **e2** the area in Center City Philadelphia; **e3** Amtrak rail yards; **e4** in front of the Aramark Global Headquarters; **e5** the Schuylkill Boardwalk, which is nearly submerged; (**e1**–**e5** credit: Mark Henninger).

but can amplify flood impacts[17–19]. While hydrodynamic models hold promise for urban flood forecasting and resilience planning, several challenges remain: limited availability of detailed terrain data, sparse observations for model calibration, difficulties in integrating heterogeneous datasets, and trade-offs between computational efficiency and storage for fine-scale simulations[20–22].

Here, we develop a high-resolution flood modeling framework for the Philadelphia-Schuylkill system, employing the Graphics Processing Unit (GPU)-accelerated LISFLOOD-FP numerical framework[23], to resolve street-level inundation dynamics. Our findings reveal a dual amplification of flood risk driven by urbanization: impervious surfaces increase runoff by reducing infiltration, while engineered infrastructure forms drainage bottlenecks that impede flow toward major waterways. We also identify Hurricane Ida's disproportionate impact on both low- and high-income populations, who experienced comparable flood exposure—underscoring the need for targeted protection of vulnerable communities. We find that the Schuylkill River's current 100-year flood capacity ($Q_{100} \approx 3,480 m^3/s$) represents a tipping point: surpassing it triggers nonlinear increases in inundation extent. Additionally, climate change and urbanization have compressed return periods, as revealed by our frequency analysis. Flows once considered 1-in-50-year events (e.g., $2,000 m^3/s$ in the 1950s) now occur statistically every 3 years. Rainfall and topography primarily govern flood patterns, whereas tidally modulated downstream water levels can further expand inundation in riparian areas. While these findings provide critical guidance for city managers, planners, and policymakers in Philadelphia, the challenges we uncover and tackle are in fact representative of riverine and coastal cities globally, each influenced by their own distinct urban landscape, environmental, and socio-economic contexts.

Results

Modeling framework

Our model integrates the city's first 5-m LiDAR-derived terrain model and the latest Schuylkill River bathymetry survey (SI Fig. S3) to best calculate flow direction. Surface roughness is calibrated using the National Land Cover Database based on the relationship between frictional Manning coefficients and land use ("Methods"). The model solves for the interaction among upstream river flow, downstream tidal elevation, and rainfall across the domain, using these three primary boundary conditions. The outputs include water depth, flow velocity, and discharge.

To validate the model's ability to reproduce flooded areas within the floodplain, we used citizen-reported data, drone and satellite imagery, and on-site observations. High-resolution drone images from Hurricane Ida show striking agreement with simulated inundation, particularly along the east bank of the Schuylkill River near Center City, where the model captures severe flooding across Fairmount Park, the museum and financial districts, and major transport corridors (Fig. 1d, e). Using satellite-based flood extent and in situ hydrodynamic measurements, we further estimate that the model reproduces 68% of inundated urban areas and more than 90% of river discharge and water levels along the channel, providing robust support for its application to compound flood risk in dense river–city systems.

Uncovering the Ida flood footprint in Philadelphia

Like many cities built along tidally influenced rivers, Philadelphia's flood severity is shaped by three key factors: watershed rainfall, river discharge, and tidal surges. The Fairmount Dam marks the upstream tidal limit of the Schuylkill River (Fig. 1c). Downstream, the tidally affected reach flows between Center City to the east and major hospitals and universities to the west, flanked by dense transportation infrastructure (Fig. 1d). Our analysis reveals that the east bank is particularly vulnerable to flooding due to its lower elevation, direct connectivity to roadways and tunnels, and localized erosion. This risk is most pronounced in the central region of the Lower Schuylkill (Fig. 1d).

Flooding also significantly impacted transportation infrastructure. Nearly all railway lines adjacent to the river experienced disruption: east bank lines, situated closer to the channel, were primarily affected by overbank flow, while west bank lines were more susceptible to intense rainfall (Figs. 1e3–5). The convergence of fluvial and pluvial drivers created a substantial hazard, particularly along the east bank, with floodwaters extending into the urban core.

But why was Hurricane Ida's impact in Philadelphia so severe? Extensive impervious surfaces and pre-saturated soils likely intensified surface runoff, increasing river discharge. These conditions highlight the role of urbanization and antecedent hydrometeorological states in amplifying flood severity during extreme events.

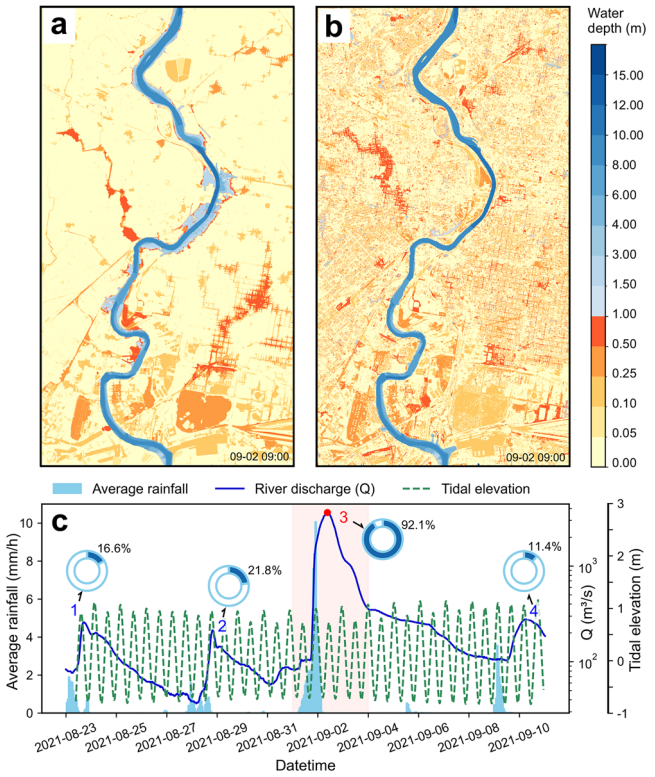

Fig. 2 | Inundation map resulting from Hurricane Ida using different elevation models. Flood inundation based on DTM (**a**) and DSM (**b**) at 9 a.m. on September 2, 2021, shown as the red point in **c**. **c** Time series of average rainfall for the whole upstream watershed, river discharge at the upstream boundary condition, and tidal elevation at the downstream boundary condition. The numbers along the discharge line correspond to four distinct peaks in river discharge, with the adjacent doughnut charts illustrating the respective runoff coefficients. Each complete doughnut chart represents the cumulative rainfall leading up to each peak, while the blue-shaded portion depicts the proportion of that rainfall converted into surface runoff. The light-orange-shaded area indicates the occurrence of the extreme rainfall event, which took place between September 1 and September 3, 2021.

Urbanization and prior hydrometeorology shaping flood risk

To examine the role of urbanization in the flood severity, we conducted numerical simulations of the Lower Schuylkill River during Hurricane Ida (September 1–3, 2021) using two digital elevation models: a bare-earth Digital Terrain Model (DTM) and an infrastructure-inclusive Digital Surface Model (DSM) (Fig. 2a, b; SI Text 2). The DTM-based simulation reveals more extensive riverine flooding, with surface runoff naturally concentrating along topographic lows and channel networks. In contrast, the DSM simulation—incorporating buildings, roads, and levees—exhibits less overbank flooding but broader distributed inundation across the urban landscape.

This spatial pattern reflects two key effects of urbanization. First, engineered riverbanks and levees constrain lower-Return-Period floods, reducing overtopping and limiting floodplain spread. Second, impervious surfaces and built structures impede drainage, trapping water in depressions and generating localized, stagnant flooding. These shallow inundations disproportionately affect pedestrian and vehicular mobility in low-lying urban neighborhoods. Overall, the DSM scenario (Fig. 2) results in a 30% increase in inundated area and an ~8% increase in downstream peak flow (SI Fig. S5) relative to the DTM (Fig. 2), underscoring the combined influence of urban form and topography on flood hazards in cities such as Philadelphia.

In addition to reduced infiltration caused by urbanization, antecedent soil moisture critically influences flood severity during EHMEs. Prior to Hurricane Ida, two moderate storms (events 1 and 2 in Fig. 2c) progressively saturated the watershed. We assessed infiltration-runoff dynamics using the runoff coefficient ($\mathcal{C}$), defined as the fraction of precipitation converted to surface runoff (SI Text 5). Four discharge peaks were analyzed: "peak 1" and "peak 2" before Ida, "peak 3" during the main flood, and "peak 4" after recession. Although rainfall before "peak 2" was lighter than before "peak 1", it generated more runoff, indicating that the 4-day dry interval was insufficient for the soil to recover its infiltration capacity. This suggests that soils were already near saturation 3 days before Ida. Consequently, nearly all rainfall during the main event was converted to runoff. While cumulative rainfall before "peak 3" was only 5.5 times that of "peak 2", river discharge was 23.2 times greater, corresponding to a peak $\mathcal{C}$ of 92.1%. One week later, $\mathcal{C}$ it dropped below 12.0%, signaling a return to baseline hydrologic conditions. These findings highlight the critical role of antecedent hydrologic conditions in shaping EHME-induced flooding. Ignoring pre-event soil moisture can lead to substantial underestimation of runoff and flood severity in urban flood models.

The strong influence of both urban form and hydrologic state on inundation patterns raises a pressing question for impact assessment and climate adaptation: Who is most at risk during extreme weather events? This concern is especially acute in densely populated cities with socio-economic disparities and aging infrastructure, where compound flooding can exacerbate vulnerabilities and amplify inequities.

Flood inequality and economic impacts in Philadelphia

We quantified individual-level flood risk using a Socioeconomic Vulnerability Index (SEVI) that averages eight indicators—housing burden, language, educational attainment, age, race, employment status, and poverty—following[24] (Fig. 3a; "Methods"). The SEVI serves as a proxy for socioeconomic status and stratifies residents into five groups. Across groups, housing burden, low educational attainment, and racial discrimination contribute most, whereas age contributes least to this study site.

Our analysis reveals that both the lowest and highest SEVI groups are disproportionately vulnerable to flooding. Despite accounting for relatively small shares of the total inundated area, these groups exhibit the highest rates of population exposure—over 20% in both cases (Fig. 3b). For high-SEVI communities, heightened exposure likely stems from insufficient flood preparedness and systemic neglect of environmental protections[25]. In contrast, low-SEVI populations face increased flood risk due to extensive impervious surfaces and localized land subsidence (measured at 1–3 mm per year) driven by groundwater withdrawal and compaction from dense infrastructure[26,27]. While proximity to water bodies offers low-SEVI residents recreational and aesthetic benefits, it also amplifies their exposure to fluvial hazards. Moreover, flooding in these economic hubs, such as Center City, can lead to substantial indirect losses, including business disruptions, and infrastructure damage that delay post-disaster recovery.

In terms of total flood-affected area, the 40–60% SEVI group experienced the most widespread inundation, reflecting that most census tracts within this study site fall in this socioeconomic vulnerability range in Philadelphia relative to Pennsylvania. Beyond these densely populated regions, urban green spaces such as Fairmount Park and FDR Park serve a dual function: providing essential recreational and cultural access while acting as natural hydrological buffers. These parks mitigate downstream flood impacts by absorbing and temporarily storing stormwater. However, during sequences of moderate rainfall followed by extreme events, their storage capacity may be exceeded, leading to increased surface runoff and more severe floods.

To better assess the economic and financial damages caused by Hurricane Ida in Philadelphia relative to other regions of Pennsylvania, we estimated the zipcode-level impact using U.S. Small Business Administration (SBA) disaster loan data[28,29] (SI Text 4). This analysis reveals a pronounced disparity in Ida's economic effects across Pennsylvania: on average, verified losses were significantly higher in Philadelphia, USD 160,061 per zipcode, while approved SBA disaster loans increased by only USD 13,997—a statistically non-significant difference (Fig. 3d). These results indicate that, although Philadelphia sustained disproportionately greater damage,

monetary support did not scale with the magnitude of its losses. The divergence between verified losses and loan disbursements indicates structural limitations in post-disaster financial mechanisms, particularly in dense urban areas where exposure and damage intensity are highest (SI Tables S3 and S4).

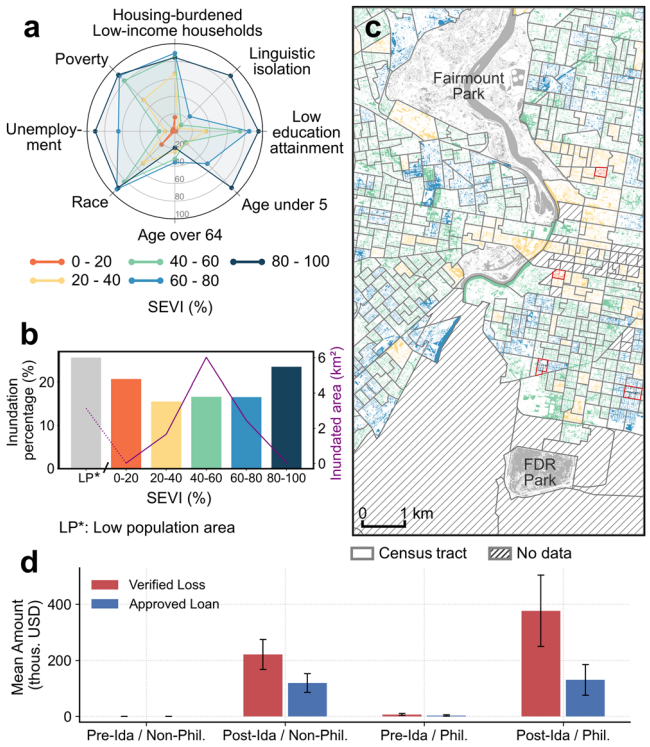

Fig. 3 | Effect of socioeconomic situation on flood inundation and economic consequences of this event. a Eight components of different socioeconomic vulnerability indices (SEVI) and their contributions in different SEVI groups. The values for each component represent the average values within each SEVI group (see "Methods"). Here, a higher SEVI indicates a more impoverished socioeconomic situation. **b** Inundation percentages and areas of different SEVI groups for this 2021 flood event. SEVI groups exclude the census tract with a population density less than 10 people per square kilometer, shown as the gray region in **c**. **c** Inundation in regions with different SEVI. Different colors indicate different SEVI groups shown in **b**. The most affected groups (0–20% and 80–100%) are highlighted with red boundaries. **d** Verified losses and approved loans in Pennsylvania Pre- and Post-Ida Hurricane. Data from the Small Business Administration US at the zipcode-year level.

These estimated impacts were further used to assess the disaster's financial implications. Across a range of discount and default rate sensitivity scenarios (SI Fig. S4, and Table S5), the resulting net present values remain consistently negative, ranging from USD 19.9 to USD 21.4 million. From a societal perspective, Hurricane Ida imposed a significant and persistent welfare loss on Philadelphia, only partially offset by existing governmental credit-based relief. Together, these findings underscore the disproportionate economic exposure of urban centers, such as Philadelphia, to climate extreme disasters and their limited financial resilience even under dedicated federal assistance programs.

Schuylkill in a changing climate

We analyzed return periods for the Schuylkill River over the past century and identified the 2021 flood as the largest fluvial event on record. The relationship between discharge and return periods follows a logarithmic trend, which we used to extrapolate peak flows for more extreme events (Fig. 4a). A more detailed examination of annual peak flows reveals a sustained upward trend, particularly for high-return-period events. Frequency analyzes of successive 20-year periods confirm this intensification (Fig. 4b, c). Although both annual peak and mean streamflow have increased significantly since 1931 (SI Fig. S6), peak flows have risen about 30 times faster than the mean. This disproportionate increase points to intensified short-duration, high-intensity rainfall events and shorter return periods for extremes. Importantly, a four-decade analysis (1970–2010) found that impervious surface across Philadelphia remained stable despite active internal land-use transitions[30]. Coupled with projections of near-consistent land types throughout the 21st century[31], these patterns offer direct evidence of climate-driven extremes in the local hydrologic regime.

To assess the implications of these trends, we simulated flood inundation across eight synthetic hydrographs, representing return periods from 5 to 5000 years. These were generated using the extrapolated discharge relationship $Q = a_0 \ln(r) + b_0$ and a standardized hydrograph based on historical events (SI Text 5, Fig. S7). Six cross-sections—three upstream and three downstream of Fairmount Dam—were selected to evaluate spatial variations of the City-River interface in response to the flood (Fig. 5a). River levels rise predictably with increasing discharge, but a sharp inflection occurs near the 100-year threshold. Below this threshold, floodwaters are typically contained within engineered riverbanks; above it, inundation expands rapidly in a logarithmic fashion (Fig. 5b), revealing the nonlinear escalation of flood hazard.

This nonlinear behavior is tightly linked to local topography and human infrastructure. During events with return periods shorter than 100 years, floodwaters remain largely confined by steep channelized banks and auxiliary structures such as raised terraces and refuge islands. However, floods with longer return periods exceed the capacity of both primary and

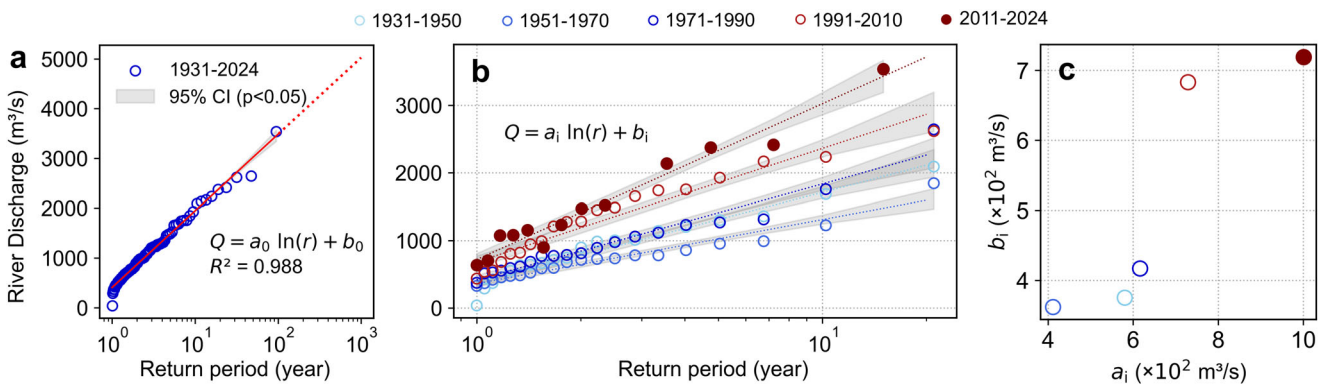

Fig. 4 | River discharge and flood inundation across different return periods. River discharge frequencies for the Schuylkill River are analyzed over the past century (**a**) and by every 20-year interval (**b**), with return periods estimated using the annual maxima series and the Weibull plotting position formula. Logarithmic trend line follows $Q = a_i \ln(r) + b_i$, with coefficients' values shown in **c**; for the full period, $a_0 = 667\ m^3/s$, $b_0 = 416\ m^3/s$. All fits yield $R_i^2 > 0.93$. Gray shaded areas indicate 95% confidence intervals.

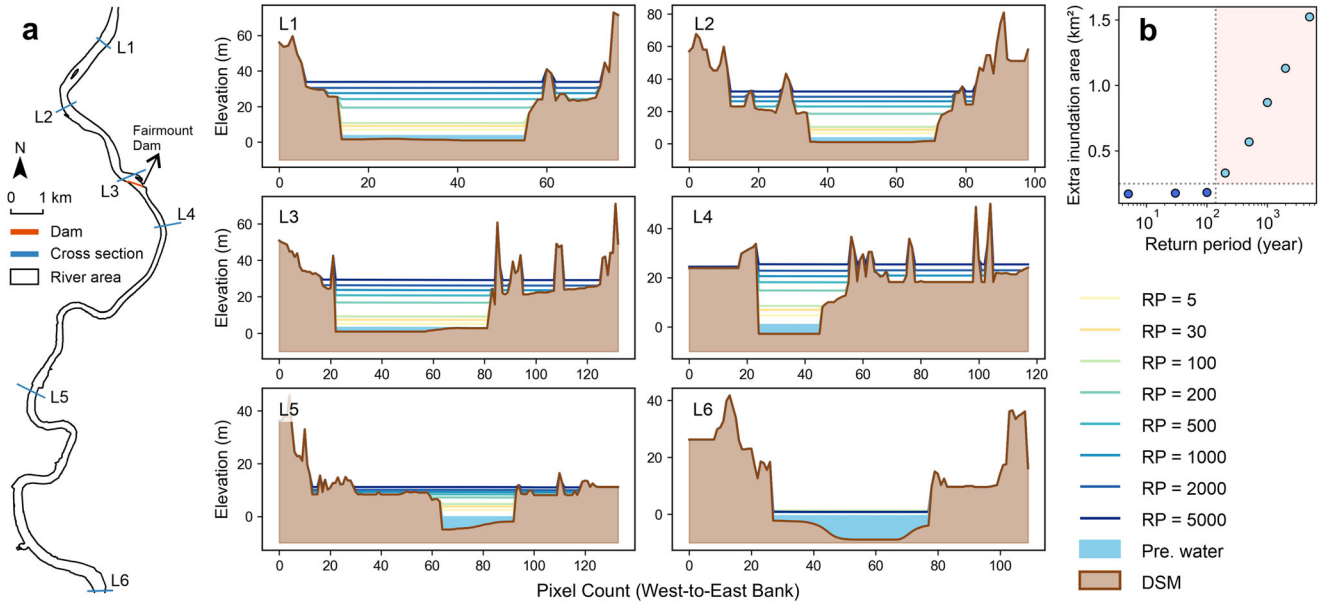

Fig. 5 | Cross sections and inundation extents of the Schuylkill River under different return periods (RP). a Top-down view of the Schuylkill River showing six selected cross sections near existing gauge stations. Three of these sections are situated upstream of the dam, while the remaining three are downstream. The "Pre. water" area represents the initial water level accumulated during the model's spin-up process. **b** River flood inundation areas for each RP, excluding the surface area of the Schuylkill River under pre-flood conditions. The light orange shaded area illustrates the logarithmic range of inundation growth, indicating that a critical flood threshold lies above the 100-year RP inflow.

secondary defenses, inundating wider urban areas (Fig. 5, panels L1–L6). Given the documented rise in extreme discharges (Fig. 4b, c), what is currently classified as a 100-year flood may become significantly more frequent. This evolving threat is compounded by tidal dynamics and SLR, which amplify overbank flooding and extend inundation into areas previously considered low risk.

Tides and sea level rise (SLR)

The interaction between the flood wave triggered by Hurricane Ida and a low but rising tide (Fig. 2c, "peak 3") raises the question of how downstream surface water elevation $\eta(t)$—modulated by tides at short timescales and SLR over long timescales—influences flood extents along the Lower Schuylkill River.

To quantify tidal influences, we performed spectral analysis of $\eta(t)$ over a 2-year period, identifying dominant tidal constituents and their key properties: amplitude, phase, and period (SI Text 6, Fig. S8). Semi-diurnal tides emerged as the primary drivers of variability, producing daily fluctuations that shift with the 14.7-day spring–neap cycle (SI Fig. S9). We also detected the annual King tide, which sets extreme tidal conditions downstream of Fairmount Dam. Because tidal stage and river discharge are statistically independent (SI Fig. S11), we applied harmonic analysis to reconstruct tidal behavior and assess compound flood risk scenarios (SI Text 8). We simulated worst-case flooding by combining the King tide with projected SLR trajectories.

Under projected SLR scenarios for 2100[32], the expansion of inundation in a 100-year flood is limited, suggesting that flows are less likely to exceed the tipping point when only coastal drivers are considered. In contrast, for a 1000-year flood event, an additional 100,000 m^2 could be inundated along the Schuylkill River (Fig. 6a), potentially affecting 5–12 city blocks or over 200 properties. To quantify the effect of extreme tide conditions on fluvial flooding, we computed the difference of inundated areas driven by the highest and lowest tide amplitude over a year. This difference increases sharply for return periods between 100 and 1000 years (Fig. 6b), primarily because the flood wave is less restricted after overtopping engineered levees and spreads through floodplains before reaching secondary barriers (Fig. 6c). On the west bank, natural terraces provide this secondary barrier, while on the east bank, a combination of built structures and elevated landforms—especially in the river's upper reach—play this role. Once floodwaters reach the second barriers, the floodplain becomes fully submerged, and additional tidal influence has a limited effect, as indicated by the leveling off inundated area beyond the 1000-year return period.

Overbank flow analysis along the tidally influenced reach (Fig. 6d) reveals consistently higher flood vulnerability on the east bank, corroborating both drone observations and model results from Hurricane Ida. The west bank, on the other hand, especially between 2 and 4.2 km, remains comparatively protected. A critical high-risk zone emerges near 2.2 km on the east bank, between the Vine Street Corridor (Fig. 1e2) and Market Street Bridge, where SLR amplifies flood risk to underground transportation infrastructure. These findings underscore the spatial variability of tide-modulated flood hazards and highlight the importance of targeted, site-specific adaptation strategies along the Lower Schuylkill River.

Changing storm characteristics

Past studies[33] have demonstrated that projected changes in tropical cyclone storm surges add to sea level rise in increasing coastal risk along the U.S. mid-Atlantic coast. Using a tropical cyclone down-scaling method driven by large-scale climate model simulations, Garner et al.[33] found that increases in both hurricane intensity and hurricane size (as measured by radius of maximum wind) contribute to increased likelihood of very large storm surges with continued warming. They focused specifically on New York City's Battery Park and the likelihood of future Superstorm Sandy-like inundation events, the return period of which is estimated to decrease from ~25 years today to ~5 years mid-century in a fossil fuel-intensive policy scenario. A similar analysis could be applied to the Schuylkill River catchment to assess the combined role of sea level change and changing storm characteristics in future projected coastal flooding risk for the Schuylkill watershed.

Discussion

Hurricane Ida produced record flooding on the Schuylkill—a nominal 1-in-100-year event. Century-scale records show such extremes are becoming more frequent and intense, with peak flows shifting from spring snowmelt to late-summer, often tropical, storms. These trends demand climate-informed risk assessment.

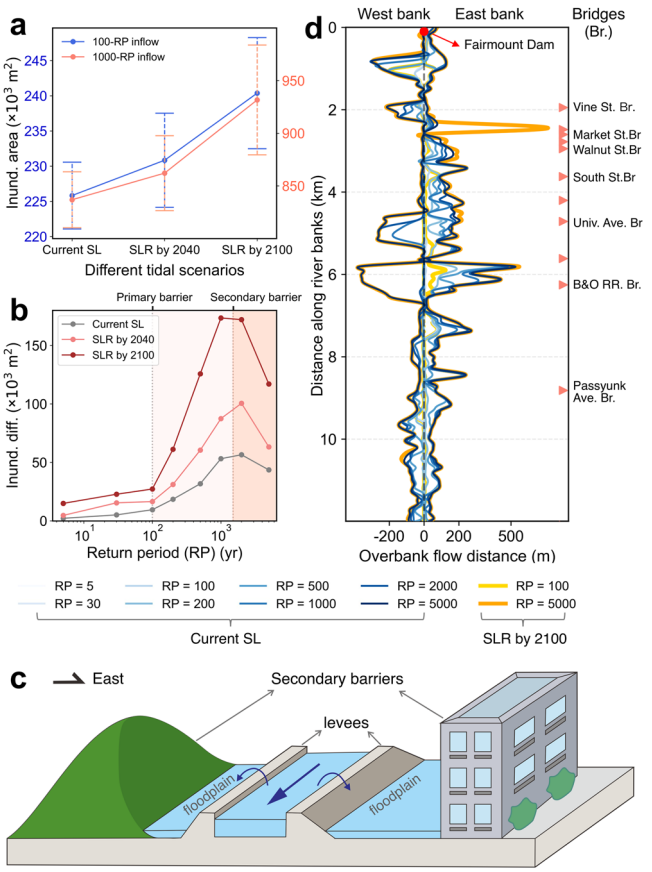

Fig. 6 | The impact of tidal phases and levels on inundation patterns and their combined effect with river discharge under different return periods (RP). a The scatter plot shows the average inundated area under 100-year and 1000-year RP river inflows, with dashed lines representing the range of inundation caused by extreme tides conditions, i.e., between the lowest and the King tide. In most cases, the largest inundated areas correspond to King tide conditions, and the lowest areas align with the lowest tide. Projected sea level rise (SLR) is based on localized estimates along the Delaware River, with increases of 0.5 meters by 2040 and 1.4 m by 2100[32]. **b** Differences in inundated area between King tide and the lowest tide in 2021 are shown across various river inflow RPs. The King tide and the lowest tide were aligned with the river discharge peak in the corresponding hydrograph for each simulation. **c** Schematic diagram of the primary and secondary barriers. **d** Overbank flow distance for various RPs river flows within the tidally affected section of the river. Distance along the river (*y*-axis) is measured relative to the Farimount Dam. Bridge names on the right are used for positioning (see SI Table S6 for full names).

Urbanization and wet antecedent soils amplify floods: impervious cover curtails infiltration and fragments flow paths, producing localized pooling rather than the channelized flooding typical of rural basins[34]. However, the detailed mechanisms of which parameters affect infiltration and recovery dynamics need further investigation. As heavy rain-bands move inland[35], cities like Philadelphia face more fluvial flooding—even without local rain. In our simulations, levees and embankments contain moderate events while buildings act as secondary barriers; once flows exceed the 100-year level, inundation expands rapidly. Designed for stationary hydrology, these defenses under-perform in a changing climate[36]. A ~30 mm storm (~2 mm/h) can take ~1 week to drain, so closely spaced storms saturate soils, boost runoff, and stress storm-water systems. Despite omitting subsurface drainage, the model reproduces Ida-driven flooding and identifies priority upgrade areas.

Our modeling framework integrates land use, urban infrastructure, rainfall, river discharge, and tides, but several uncertainties constrain our inferences. Near-term upgrades include spatially variable infiltration, explicit subsurface drainage, and wind effects on river dynamics and surge. Evaporation was neglected, given its small contribution (~0.3% of basal discharge). Morphology is static, though extreme flows can reshape channels[37,38]. On the Schuylkill, suspended sediment concentration rises sharply once riverbed shear exceeds ~24 Pa (discharge > 100m^3/s, SI Fig. S10); sediment records cover less than 10 years (1959–1968), underscoring monitoring gaps (SI Text 7).

Given these bounds, compound controls remain decisive in the tidally influenced Lower Schuylkill: risk spikes when river peaks coincide with high tide, and SLR amplifies this hazard. With ~1.4 m SLR by 2100, a 100-year flood could expand inundation by up to 15%, with larger increases for rarer events. Flood extent and pathways reflect hydrology and the built environment; mapping these constraints reveals hotspots and areas where riverine risk shifts to rainfall-driven flooding. Neighborhoods > 500 m from the river generally face lower fluvial exposure, though local topography and drainage still govern residual risk (SI Fig. S12).

Effective risk reduction requires geographically tailored strategies. The east bank's proximity to major roads and transit concentrates riverine exposure; the higher west bank's flat lands and rail yards are more prone to pluvial flooding. Both high- and low-income groups are exposed, but in different ways: higher-income riverfront and Central Business District can face elevated exposure from subsidence and infrastructure loading, while lower-income communities may lack preparedness resources and experience prolonged recovery, including public-health risks from sewage contamination[39]. Quantitative assessments of long-term socio-economic impacts (displacement, unemployment, educational disruption, mental health) remain scarce[25].

Despite data constraints—especially acute in under-resourced regions[21]—hydrodynamic models remain essential for resilience planning under evolving hydrometeorology[40,41]. Rising peak discharges for a given return period and pervasive SLR argue for climate-adaptive, not fixed-in-time, infrastructure to attenuate flood waves[42–44]. Nature-based solutions (e.g., Fairmount Park and FDR Park as stormwater "sponges") can cost-effectively complement gray systems[45,46]. Expanding access to high-resolution topography, precipitation forecasts, and high-performance modeling enables robust, real-time flood forecasting to protect vulnerable populations and critical assets. Philadelphia's priorities are: (i) compound-aware standards for capital projects (joint rainfall–river–tide–SLR design events; updated maps/codes); (ii) green–gray hybrids—floodable open spaces and expanded storage in Fairmount and FDR Parks—paired with hardened utilities and rail yards[45,46]; (iii) real-time forecasting using high-resolution topography and ensemble precipitation; and (iv) equitable adaptation that directs investment where hazard intersects socioeconomic vulnerability, and prioritizes critical services in frontline neighborhoods. Closing sediment, morphology, and drainage data gaps will reduce model uncertainty and sharpen prioritization[42–44].

We present a general approach to map flood risk from climate extremes in urban riverine systems. Using the Philadelphia–Schuylkill system as an example, we show that compound interactions among river discharge, tides/SLR, and the built environment recur across coastal cities, offering a transferable framework for site-specific, equitable adaptation.

Methods

LISFLOOD-FP model description

LISFLOOD-FP numerical solver is a 1D-2D raster-based hydrodynamic model based on the shallow water equations[23] (SI Text 1), which enable the modeling of spatially and temporally varying processes like precipitation and local water discharges; it can be directly downloaded from Zenodo (https://zenodo.org/records/6912932). Here, we used the state-of-the-art acceleration hydrodynamic solver LISFLOOD-ACC[23] as a local inertial scheme to numerically resolve the water flow throughout a uniform grid describing the urban landscape, the floodplain, and the river channel[47,48]. This solver has been shown to have high fitting accuracy with real inundations and runs with NVIDIA GPU cores to significantly enhance the computational efficiency[23].

Watershed landscape and friction

The hydraulic resistance encountered by the river flow due to the land surface characteristics and the riverbed's composition is quantified by Manning's frictional coefficient (n). This coefficient exhibits spatial variability and undergoes minor temporal changes. To establish the spatial distribution of the Manning coefficient within our study area, we have leveraged the United States Geological Survey (USGS) National Land Cover Dataset to analyze the current land use following[49]. The determined Manning coefficient ranges from 0.027 to 0.160. This detailed mapping of the landscape friction allows capturing the subtle variability in hydraulic resistance across the urban watershed of the Lower Schuylkill River (SI Fig. S14).

River discharge analysis

We conducted a frequency analysis to determine return periods for the Schuylkill River using historical peak discharge data from 1931 to 2024. Data prior to 1990 were based on the peak of daily average discharge, owing to the lower temporal resolution at that time, resulting in slight smoothing of peak values. Data from 1991 onward utilized peak flow values derived from 30-min interval measurements. When comparing peak flows across consecutive 20-year periods, the return period was recalculated because it is correlated with the length of the dataset (SI Text 5).

We used a long-time series of river discharges to analyze the single-peaked hydrograph of the Schuylkill River and further design flood hydrographs of more severe river scenarios. The time when the river flow peaks is defined as the origin, with time values before and after, negative and positive, respectively. The river discharge was scaled to 0 to 1 based on its proportion in the peak flow. The shape of a single-peaked hydrograph of the Schuylkill River is generally similar, so we assumed self-similarity in extrapolating flood waves to higher return periods. Rainfall intensities and associated river flows tend to follow the Gamma distribution[50]. However, this distribution does not capture the recession limb of river flows, so exponential functions are used to model the withdrawal of flows[51]. Two equations based on the gamma distribution and exponential function, respectively, were used to fit the shape of the hydrograph (SI Text 5). The hydrograph for a higher return period is designed by multiplying the fitted function by the calculated peak flow for a given return period based on the "similar-shape" assumption.

Tidal analysis

We used the Lomb-Scargle Periodogram Analysis, a spectral-density analysis method that is suitable for unequally spaced datasets[52], to detect the frequency of periodic signals of the Schuylkill River within the latest 2 years of tidal elevation data. Our results showed that the Schuylkill River is dominantly tidally modulated by the Lunar (M_2) and the Solar (S_2) semi-diurnal tides, and K_1 and O_1 diurnal tide. Thus, we used four Fourier modes to fit and model the tidal elevation signal as a function of time:

$$\eta(t) = \eta_0 + \sum_{i=1}^{4} A_i \sin\left[2\pi \frac{(t + t_0)}{T_i} + \phi_i\right], \quad (1)$$

$$t_0 = \mathrm{T}_0\,(\mathrm{TP}_i - \mathrm{TP}_0). \quad (2)$$

where $\eta_0 = 0.074$m. A_i, T_i, and ϕ_i are the amplitude, period, and phase of each tidal constituent, with values shown in SI Table S7. t_0 is 0 in the real flood case, yet it varies based on different TPs. TP_i represents a different tidal phase (SI Fig. S13), while TP_0, equal to 0.42, is the phase during the real event. T_0 in Eq. 2 is a constant representing the semidiurnal period, approximately equal to 0.5 days.

To assess the relationship between river peak discharge and tidal levels, we computed Spearman and Kendall rank correlation coefficients. Both values indicate statical significance (Spearman = −0.124, $p = 0.009$; Kendall = −0.086, $p = 0.007$), yet their low magnitudes ($|r| < 0.13$) suggest a negligible association. Thus, the two variables can be considered approximately independent for modeling purposes (see SI Fig. S11, SI Text 8.1).

Socioeconomic vulnerability index (SEVI)

The SEVI is the average value of eight socioeconomic components, which are percentile values calculated for each census tract based on the distribution of all values across Pennsylvania. We excluded low-population-density areas when analyzing inundation for different SEVI groups to avoid misleadingly favorable Socioeconomic conditions. The value of the inundation percentage was calculated by dividing the total inundation area in each SEVI group by the total census tract areas in the same SEVI group.

The socioeconomic statistics were analyzed based on the 2010 census block groups rather than the latest 2020 groups to ensure consistency, as specific components still rely on the 2010 census geometries. However, since the latest demographic data is based on 2020 census block groups, we assumed that the population density within the same census tract remains consistent regardless of location. We then recalculated the population density for these mismatched groups using their respective area proportions. This estimate had minimal impact on the detection of low-population areas.

Model validation

The model was challenged and well validated using three methods. First, the overall inundation was qualitatively compared with a single Sentinel-2A MSI Level-2A (atmospherically corrected) image, the only satellite product with acceptable cloud cover during this flooding event. We used the water indices AWEIsh[53] to extract the inundation area and set a 15-cm water depth threshold to consider a wet cell[54] and quantify the inundation area. The "Hit rate" for the DTM and DSM modeling results is 0.51 and 0.68, respectively, indicating positive correspondence. This suggests the model adeptly captures the river channel expansion, even though there is a tendency to overpredict the flood severity, particularly in urban areas. This overprediction aligns with expectations since the model excludes infiltration and drainage networks.

Second, we used the model skill metric (MSM) to assess the model's performance in predicting river discharge and surface elevation[55] (SI Text 3). The MSM s' results consistently exceed 90% (SI Table S1), affirming the model's exceptional ability to reproduce river hydrodynamics accurately.

Last, we used drone images with landmarks to compare the actual inundation extent with the model's predictions. This analysis revealed a strong alignment between the observed and modeled inundation areas, indicating the model's accuracy in representing real-world conditions.

Data availability

River discharge upstream of the Fairmount Dam, at station PA-0147500, is obtained from the USGS water database (https://waterdata.usgs.gov/monitoring-location/01474500/). Tidal elevation downstream is available from a National Oceanic and Atmospheric Administration (NOAA) tide gauge (PA-8543925) (https://tidesandcurrents.noaa.gov/noaatidepredictions.html). Hourly precipitation grids were provided directly by the Office of Hydrological Development, NOAA. 1-meter Digital terrain model (DTM), named as 3D Elevation Program (3DEP), was available from USGS TNM Service (https://apps.nationalmap.gov/downloader/). Newly released LiDAR point cloud data, used to generate Digital Surface Model (DSM), is available from a Philadelphia LiDAR survey (https://geo.btaa.org/catalog/pasda-7154). River bathymetry data was collected from the latest Lower Schuylkill survey provided by the US Army Corps of Engineers Philadelphia (https://www.nap.usace.army.mil/Missions/Civil-Works/Surveys/Projects/). Surface landscape is available from National Land Cover Database (NLCD) 2021 (https://www.usgs.gov/centers/eros/science/national-land-cover-database). Census tracts 2020, the boundary files of districts and watersheds in Philadelphia can be downloaded from Open Data PHLmaps (https://data-phl.opendata.arcgis.com/datasets/). Demographic data on census-tract level is available from 2017-2021 American Community Survey 5-Year Estimates on U.S. Census Bureau (https://data.census.gov/table/). The latest Environmental justice

dataset can be downloaded from PA Department of Environmental Protection (https://gis.dep.pa.gov/PennEnviroScreen/). U.S. Small Business Administration (SBA) dataset loss and loan datasets from 2000 to 2022 are available at https://data.sba.gov/en/dataset/disaster-loan-data. The OpenFEMA dataset of disaster declarations summaries can be downloaded from the official website of the U.S. Department of Homeland Security at https://www.fema.gov/openfema-data-page/disaster-declarations-summaries-v2. The Sentinel-2 satellite image is available from Copernicus Browser (https://browser.dataspace.copernicus.eu/). The road network dataset is available from U.S. Census Bureau, Department of Commerce (https://catalog.data.gov/dataset/).

Code availability

Codes are available at https://doi.org/10.5281/zenodo.17055415[56] to reproduce our results.

Received: 9 December 2025; Accepted: 12 February 2026;
Published online: 25 February 2026

References

1. Zhu, Y.-J., Collins, J. M., Klotzbach, P. J., Schreck, C. J. & Hurricane, I. da (2021): Rapid intensification followed by slow inland decay. *Bull. Am. Meteorol. Soc.* **103**, E2354–E2369 (2022).
2. United Nations University - Institute for Environment and Human Security (UNU-EHS), Higuera Roa, O. & O'Connor, J. *Technical Report: Hurricane Ida*. http://collections.unu.edu/view/UNU:9023 https://doi.org/10.53324/NYKY2894 (2022).
3. Centre for Research on the Epidemiology of Disasters (CRED). *2023 Disasters in Numbers: A Significant Year of Disaster Impact*. https://files.emdat.be/reports/2023_EMDAT_report.pdf (2024).
4. NOAA National Centers for Environmental Information (NCEI). U.S. Billion-Dollar Weather and Climate Disasters. NOAA https://www.ncei.noaa.gov/access/billions/ (2025).
5. IPCC. IPCC, 2023: Climate Change 2023: Synthesis Report. Contribution of Working Groups I, II and III to the Sixth Assessment Report of the Intergovernmental Panel on Climate Change [Core Writing Team, H. Lee and J. Romero (Eds.)]. IPCC, Geneva, Switzerland. https://www.ipcc.ch/report/ar6/syr/ https://doi.org/10.59327/IPCC/AR6-9789291691647 (2023).
6. Zhang, W., Villarini, G., Vecchi, G. A. & Smith, J. A. Urbanization exacerbated the rainfall and flooding caused by Hurricane Harvey in Houston. *Nature* **563**, 384–388 (2018).
7. Jing, R. et al. Global population profile of tropical cyclone exposure from 2002 to 2019. *Nature* **626**, 549–554 (2024).
8. Ghanbari, M., Arabi, M., Kao, S., Obeysekera, J. & Sweet, W. Climate change and changes in compound coastal-riverine flooding hazard along the U.S. coasts. *Earths Future* **9**, e2021EF002055 (2021).
9. Wing, O. E. J. et al. Estimates of present and future flood risk in the conterminous United States. *Environ. Res. Lett.* **13**, 034023 (2018).
10. Sharma, A., Wasko, C. & Lettenmaier, D. P. If precipitation extremes are increasing, why aren't floods?. *Water Resour. Res.* **54**, 8545–8551 (2018).
11. Lopes, C. L. et al. Evaluation of future estuarine floods in a sea level rise context. *Sci. Rep.* **12**, 8083 (2022).
12. Slater, L. J. & Villarini, G. Recent trends in U.S. flood risk. *Geophys. Res. Lett.* **43**, 12428–12436 (2016).
13. Scharf, J. T. & Westcott, T. *History of Philadelphia, 1609–1884*. Vol. 1 (L. H. Everts & Company, Philadelphia, 1884).
14. Interlandi, S. J. & Crockett, C. S. Recent water quality trends in the Schuylkill River, Pennsylvania, USA: a preliminary assessment of the relative influences of climate, river discharge and suburban development. *Water Res.* **37**, 1737–1748 (2003).
15. Gori, A., Lin, N., Xi, D. & Emanuel, K. Tropical cyclone climatology change greatly exacerbates US extreme rainfall–surge hazard. *Nat. Clim. Change* **12**, 171–178 (2022).
16. Balaguru, K. et al. Increased U.S. coastal hurricane risk under climate change. *Sci. Adv.* **9**, eadf0259 (2023).
17. Orton, P. M. et al. Flood hazard assessment from storm tides, rain and sea level rise for a tidal river estuary. *Nat. Hazards* **102**, 729–757 (2020).
18. Jang, J.-H. & Chang, T.-H. Flood risk estimation under the compound influence of rainfall and tide. *J. Hydrol.* **606**, 127446 (2022).
19. Moftakhari, H. R., Salvadori, G., AghaKouchak, A., Sanders, B. F. & Matthew, R. A. Compounding effects of sea level rise and fluvial flooding. *Proc. Natl. Acad. Sci. USA* **114**, 9785–9790 (2017).
20. Teng, J. et al. Flood inundation modelling: a review of methods, recent advances and uncertainty analysis. *Environ. Model. Softw.* **90**, 201–216 (2017).
21. Bates, P. Fundamental limits to flood inundation modelling. *Nat. Water* **1**, 566–567 (2023).
22. Kumar, V., Sharma, K., Caloiero, T., Mehta, D. & Singh, K. Comprehensive overview of flood modeling approaches: a review of recent advances. *Hydrology* **10**, 141 (2023).
23. Sharifian, M. K., Kesserwani, G., Chowdhury, A. A., Neal, J. & Bates, P. LISFLOOD-FP 8.1: new GPU-accelerated solvers for faster fluvial/pluvial flood simulations. *Geosci. Model Dev.* **16**, 2391–2413 (2023).
24. Besse, H. & Rojas-Rueda, D. Environmental justice mapping tools in the United States: a review of national and state tools. *Sci. Total Environ.* **962**, 178449 (2025).
25. Hino, M. & Nance, E. Five ways to ensure flood-risk research helps the most vulnerable. *Nature* **595**, 27–29 (2021).
26. Ohenhen, L. O., Shirzaei, M., Ojha, C., Sherpa, S. F. & Nicholls, R. J. Disappearing cities on US coasts. *Nature* **627**, 108–115 (2024).
27. Ohenhen, L. O. et al. Land subsidence risk to infrastructure in US metropolises. *Nat. Cities* **2**, 543–554 (2025).
28. Josephson, A. & Marshall, M. I. The demand for Post-Katrina disaster aid: SBA disaster loans and small businesses in Mississippi. *J. Contingencies Crisis Manag.* **24**, 264–274 (2016).
29. Collier, B., Howell, S. & Rendell, L. *After the Storm: How Emergency Liquidity Helps Small Businesses Following Natural Disasters*. w32326 http://www.nber.org/papers/w32326.pdf (2024) https://doi.org/10.3386/w32326.
30. Locke, D. H., Roman, L. A., Henning, J. G. & Healy, M. Four decades of urban land cover change in Philadelphia. *Landsc. Urban Plan.* **236**, 104764 (2023).
31. U.S. Geological Survey. *Land Change Monitoring, Assessment*, and Projection (LCMAP). https://pubs.usgs.gov/fs/2020/3024/fs20203024.pdf (2020).
32. Strauss, B. et al. *Pennsylvania and the Surging Sea: A Vulnerability Assessment with Projections for Sea Level Rise and Coastal Flood Risk* https://www.climatecentral.org (2016).
33. Garner, A. J. et al. Impact of climate change on New York City's coastal flood hazard: Increasing flood heights from the preindustrial to 2300 CE. *Proc. Natl. Acad. Sci. USA* **114**, 11861–11866 (2017).
34. Bates, P. Uneven burden of urban flooding. *Nat. Sustain.* **6**, 9–10 (2022).
35. Hoerling, M. et al. Characterizing recent trends in U.S. heavy precipitation. *J. Clim.* **29**, 2313–2332 (2016).
36. Milly, P. C. D. et al. Stationarity is dead: whither water management?. *Science* **319**, 573–574 (2008).
37. Li, A. K. et al. Towards understanding underwater weather events in rivers using autonomous surface vehicles. in *OCEANS 2022, Hampton* Roads 1–8 (IEEE, Hampton Roads, VA, USA, 2022). https://doi.org/10.1109/OCEANS47191.2022.9977236.
38. Slater, L. J., Singer, M. B. & Kirchner, J. W. Hydrologic versus geomorphic drivers of trends in flood hazard. *Geophys. Res. Lett.* **42**, 370–376 (2015).
39. Watson, J. T., Gayer, M. & Connolly, M. A. Epidemics after natural disasters. *Emerg. Infect. Dis.* **13**, 1–5 (2007).
40. Nkwunonwo, U. C., Whitworth, M. & Baily, B. A review of the current status of flood modelling for urban flood risk management in the developing countries. *Sci. Afr.* **7**, e00269 (2020).

41. Tudaji, M., Nan, Y. & Tian, F. Assessing the value of high-resolution rainfall and streamflow data for hydrological modeling: an analysis based on 63 catchments in southeast China. *Hydrol. Earth Syst. Sci.* **29**, 1919–1937 (2025).
42. Hinkel, J. et al. Coastal flood damage and adaptation costs under 21st century sea-level rise. *Proc. Natl. Acad. Sci. USA* **111**, 3292–3297 (2014).
43. Hummel, M. A., Griffin, R., Arkema, K. & Guerry, A. D. Economic evaluation of sea-level rise adaptation strongly influenced by hydrodynamic feedbacks. *Proc. Natl. Acad. Sci. USA* **118**, e2025961118 (2021).
44. Remo, J. W. F., Carlson, M. & Pinter, N. Hydraulic and flood-loss modeling of levee, floodplain, and river management strategies, Middle Mississippi River, USA. *Nat. Hazards* **61**, 551–575 (2012).
45. Jongman, B. Effective adaptation to rising flood risk. *Nat. Commun.* **9**, 1986 (2018).
46. Van Zelst, V. T. M. et al. Cutting the costs of coastal protection by integrating vegetation in flood defences. *Nat. Commun.* **12**, 6533 (2021).
47. Archer, L. et al. Current and future rainfall-driven flood risk from hurricanes in Puerto Rico under 1.5 and 2 °C climate change. *Nat. Hazards Earth Syst. Sci.* **24**, 375–396 (2024).
48. Hatchard, S., Schmitt, R. J. P., Pianosi, F., Savage, J. & Bates, P. Strategic siting and design of dams minimizes impacts on seasonal floodplain inundation. *Environ. Res. Lett.* **18**, 084011 (2023).
49. Soliman, M., Morsy, M. M. & Radwan, H. G. Assessment of implementing land use/land cover LULC 2020-ESRI global maps in 2d flood modeling application. *Water* **14**, 3963 (2022).
50. Martinez-Villalobos, C. & Neelin, J. D. Why do precipitation intensities tend to follow gamma distributions?. *J. Atmosph. Sci.* **76**, 3611–3631 (2019).
51. Goswami, M. Generating design flood hydrographs by parameterizing the characteristic flood hydrograph at a site using only flow data. *Hydrol. Sci. J.* **67**, 2505–2523 (2022).
52. VanderPlas, J. T. Understanding the Lomb–Scargle Periodogram. *Astrophys. J. Suppl. Ser.* **236**, 16 (2018).
53. Yang, X., Qin, Q., Grussenmeyer, P. & Koehl, M. Urban surface water body detection with suppressed built-up noise based on water indices from Sentinel-2 MSI imagery. *Remote Sens. Environ.* **219**, 259–270 (2018).
54. Wing, O. E. J. et al. Validation of a 30 m resolution flood hazard model of the conterminous United States. *Water Resour. Res.* **53**, 7968–7986 (2017).
55. Willmott, C. J. On the validation of models. *Phys. Geogr.* **2**, 184–194 (1981).
56. Xuan, D. & Ulloa, H. N. Compound flood modelling in the Philadelphia-Schuylkill System. Zenodo https://doi.org/10.5281/ZENODO.17478154 (2025).

Acknowledgements

The work was supported by the University of Pennsylvania's University Research Foundation (URF) Award. We greatly acknowledge the support from: the U.S. Army Corps of Engineers Philadelphia District for facilitating the latest sounding survey of the Schuylkill River, the National Weather Service Middle Atlantic River Forecast Center for providing hourly precipitation grids combining rain gauges with radar data. Leandro S. Pongeluppe gratefully acknowledges support from Leonard J. Horwitz, the Wharton Impact, and the Wharton AI & Analytics Initiative. We are grateful to Mark Henninger for generously providing drone images of the flooding triggered by Hurricane Ida in 2021, which were used in this study. We sincerely thank Dr. Jose A. Marengo for valuable scientific discussions related to this study. We thank www.wefilmphilly.com for granting access to the film "The 2021 Philadelphia Flood | Hurricane Ida", which provides rare, event-specific documentation used to benchmark our model against observed flood impacts in Philadelphia.

Author contributions

D.X., H.N.U., M.A.H., D.J.J. designed research, D.X. performed research, H.N.U. supervised research, L.S.P. contributed to economic analysis, M.M.W., M.E.M. contributed to hurricane analysis and discussion; H.N.U. acquired funding; All wrote the paper. All the authors approve the manuscript.

Competing interests

The authors declare no competing interests.

Additional information

Supplementary information The online version contains supplementary material available at https://doi.org/10.1038/s44304-026-00186-8.

Correspondence and requests for materials should be addressed to Dingyu Xuan or Hugo N. Ulloa.